Pore-to-Core Laboratory Upscaling and Visualization of Enhanced Oil Recovery and CO_2 Storage

Jarand Gauteplass

Dissertation for the degree philosophiae doctor (PhD)

at the University of Bergen

2015

Dissertation date: January 9th

Year: 2015

Title: Pore-to-Core Laboratory Upscaling and Visualization of Enhanced Oil Recovery and CO_2 Storage

Author: Jarand Gauteplass

Print: AIT OSLO AS / University of Bergen

Table of Contents

Summary

The global energy demand increases, and the need for hydrocarbon reserve growth is evident. The maturation of hydrocarbon formations worldwide combined with declining rate of major oil and gas discoveries, have caused a renewed focus on implementing enhanced oil recovery (EOR) methods in hydrocarbon reservoirs. The success of an EOR project relies on identifying the key driving forces. Non-invasive, non-perturbing imaging of fluid dynamics in laboratory opaque systems can identify recovery mechanisms beyond material balance experiments. Furthermore, flow experiments should be conducted at a variety of scales in the laboratory to couple small-scale phenomena and basic mechanisms to the complexity of fluid flow in the field. This thesis visualizes and identifies EOR mechanisms from pore- to core-scale in order to improve fluid flow characterization in porous media.

A novel imaging approach is presented in **Paper 1** where positron emission tomography (PET) to image fluid flow was combined with structural information acquired from computed tomography (CT). Superimposed images described how rock discontinuities affected labeled water fronts and overall sweep efficiency. **Paper 2** is an extension of **Paper 1** and involves explicit tracking of the gas phase and evaluates the synergy between EOR and permanent CO_2 storage. Molecular diffusion and viscous displacement were identified as recovery mechanisms in respectively fractured sandstone and tight shale. Furthermore, a large fraction of injected CO_2 was effectively retained in the pores by capillary forces, demonstrating the potential for safe CO_2 sequestration. Explicit flow information during waterfloods and CO_2 injection for EOR and storage was successfully used to evaluate size dependence on developed flow patterns.

The pore-to-core scale approach was experimentally verified in **Paper 3**, where similar displacement systems were studied at the pore-scale. Capillary and

dissolution trapping of CO_2 by water were directly observed in etched-silicon micromodels. CO_2 was trapped in single pores and in larger clusters, and the residual phase was poorly connected throughout the network. In pore-level observation of CO_2 EOR, high recoveries were observed due to a spreading oil layer between the water phase and the non-wetting gas phase.

Building on **Paper 1-3**, it was evident that CO_2 injection for EOR in fractured systems needed to be improved. Therefore, **Paper 4** evaluates mobility control in fractures. Co-injection of gas and surfactant solution was compared to water-alternating-gas (WAG) and continuous gas injection (CGI), and was the preferred method in terms of areal sweep and mobility reduction factor in 2D fracture networks as a result of foam generation. Foam generation was studied at the pore-scale in **Paper 5**, where rectilinear snap-off and snap-off at permeability discontinuities were identified as important lamella creation mechanisms.

Low salinity waterflooding (LSW) was evaluated in **Paper 6** as an alternative to gas injection in oil-wet carbonates. Wettability alteration and interfacial tension reduction between crude oil and water were effects attributed to LSW, resulting in enhanced secondary and tertiary oil recovery at reservoir conditions. Osmotic pressure was discarded as a dominant LSW mechanism in corefloods based on pore-level observations.

Acknowledgements

I wish to acknowledge the Norwegian Research Council for financial support.

I would like to express my gratitude to my supervisors, Associate Professor Martin A. Fernø and Professor Arne Graue for excellent guidance throughout the years and for providing the opportunity to work in great research environments here in Bergen and overseas.

To all my former and current associates in the reservoir physics group, thank you for excellent collaboration. A special thanks to my colleagues Øyvind Eide and Lars Petter Øren Hauge for great companionship and for sharing memorable experiences over the years.

Thanks to Reza Barati at the University of Kansas for guidance, collaboration and a nice stay in Lawrence. Thanks to Anthony R. Kovscek at Stanford University and Sibani Lisa Biswal and George J. Hirasaki at Rice University for valuable discussions on foam and microfluidic systems. Thanks to Tom Christian Adamsen and Geir Espen Abell for guidance and collaboration regarding PET/CT imaging at Haukeland University Hospital.

Thanks to the Mechanical Workshop at the Dept. of Physics and Technology for excellent craftsmanship over the years. Thanks to Rachid Maad for repairing and improving laboratory equipment.

Finally, a special thanks to my family and friends for motivation, support and great academic time-outs. It has been much appreciated!

Jarand Gauteplass

List of Publications

1. Fernø, M.A., **Gauteplass, J.**, Hauge, L.P., Abell, G.E., Adamsen T.C. & Graue, A.: "Quantitative Visualization of CO_2 Storage and Oil Recovery Using Positron Emission and X-ray Computed Tomography", submitted to *Geophysical Research Letters.*

2. Fernø, M.A., Hauge, L.P., **Gauteplass, J.**, Abell, G.E., Adamsen T.C. & Graue, A.: "Explicit CO_2 Flow Characterization in Unconventional Formations", manuscript.

3. **Gauteplass, J.**, Follesø, H.N., Graue, A., Kovscek, A.R. & Fernø, M.A: "Visualization of Pore-level Displacement Mechanisms during CO_2 Injection and EOR Processes", proceedings at *EAGE IOR 2013: From Fundamental Science to Deployment*, Saint Petersburg, Russia, 16-18 April 2013.

4. Fernø, M.A., **Gauteplass, J.**, Pancharoen, M., Haugen, Å., Graue, A., Kovscek, A.R. & Hirasaki, G.: "Experimental Study of Foam Generation, Sweep Efficiency and Flow in a Fracture Network", SPE 170840, proceedings at *SPE Annual Technical Conference and Exhibition*, Amsterdam, The Netherlands, 27–29 Oct. 2014.

5. **Gauteplass, J.**, Chaudhary, K., Kovscek, A.R. & Fernø, M.A.: "Pore-level Foam Generation and Flow for Mobility Control in Fractured Systems", submitted to the *Journal of Colloid and Interface Science*.

6. **Gauteplass, J.**, Leon, I.D., Markey F.J., Fernø, M.A., Graue, A., Barati, R.: "Low Salinity Waterflooding in Carbonates: Improved Oil Recovery and Relative Permeability Effects", submitted to *Transport in Porous Media*.

Additional Scientific Production

1. Hauge, L.P, **Gauteplass, J**., Høyland, M.D., Ersland, G., Fernø, M. & Graue, A.: "Pore-Scale Visualization of Hydrate Formation and Dissociation in High Pressure Clastic Micromodels", manuscript in preparation, to be submitted to *International Journal of Greenhouse Gas Control.*

2. Markey, F., Betz, T., **Gauteplass, J**., Taylor, K., Ackwith, D., & Barati, R.: "Examining Innovative Techniques For Matrix Acidizing In Tight Carbonate Formations To Minimize Damage To Equipment And Environment", proceedings at *Unconventional Resources Technology Conference*, Denver, USA, 25-27 Aug. 2014.

3. **Gauteplass, J**., Fredriksen, S.B., Rognmo, A.U. & Fernø, M.A.: "Osmotic Mobilization of Residual Oil during Low Salinity Waterflooding", scientific report, Statoil ASA, Norway, Jan. 2014.

4. Hauge, L.P, **Gauteplass, J**., Eide, Ø., Birkedal, K.A., Ersland, G., Fernø, M. & Graue, A.: "*In situ* Imaging of CO_2 Flow, Storage and Entrapment in Subsurface Aquifers and Hydrocarbon Reservoirs", poster at *CLIMIT Seminar*, Oslo, Norway, 2013.

5. Hauge, L.P, **Gauteplass, J**., Mathiassen, T., Kvinge, G.A., Birkedal, K.A., Ersland, G., Fernø, M., Graue, A., Ramstad, T., Rueslåtten, H.: "Pore-scale Modeling and *In situ* Imaging of CO_2 Injection in Brine Saturated Sandstone", poster at *CLIMIT Seminar*, Oslo, Norway, 2013.

6. **Gauteplass, J**., Fernø, M.A, Follesø, H.N. & Graue, A.: "Pore-Level Fluid Displacement Mechanisms in Etched Silicon Wafer Micromodels", poster at *Transatlantic Science Week*, Houston, USA, 2012.

1. Theory and Background

A theoretical background on hydrocarbon production schemes and enhanced oil recovery (EOR) methods emphasizing improved volumetric sweep efficiency are presented in this chapter. Here, the potential for EOR by CO_2 injection combined with CO_2 storage in the reservoir, as well as mechanisms involved in low salinity waterflooding and foam injection are discussed. In addition, imaging techniques used in the included scientific papers are briefly reviewed.

1.1 Introduction

The focus on enhanced oil recovery (EOR) has recently gained renewed interest as a result of current high oil prices, maturation of hydrocarbon formations worldwide, few new major oil and gas discoveries, and the increasing global energy demand. EOR is defined as oil production through the injection of energy and fluids not normally present in the hydrocarbon formation (Lake, 1989). The main objective of all EOR methods is to increase the macroscopic sweep efficiency and the microscopic displacement efficiency compared to conventional recovery, e.g. waterflooding. EOR mechanisms include mobility control and selective plugging, oil swelling, oil viscosity reduction, water thickening, interfacial tension reduction between displaced and displacing fluid, miscible displacement, and fluid-rock interactions leading to wettability alterations.

Injection strategies are affected by field location, reservoir structure, rock wettability, reservoir pressure and temperature, conventional or fractured reservoir, initial fluid distribution, reservoir fluid properties and oil/gas prices among other. Especially in naturally fractured reservoirs (often oil-wet carbonates), achieving acceptable volumetric sweep can be challenging due to large permeability contrasts. Foam has the potential to increase gas flow resistance in high permeable fractures and divert gas into regions of lower permeability. Another example of improved sweep is during low salinity

waterflooding, where wettability alteration can lead to spontaneous imbibition of water in areas having established positive capillary pressure.

1.2 CO_2 Injection

Applications for carbon dioxide (CO_2) injection include enhanced oil recovery, methane production from hydrate-bearing formations, and CO_2 storage in depleted hydrocarbon reservoirs and deep saline aquifers. Carbon capture utilization and storage (CCUS) has emerged as a method to counteract part of the CO_2 emissions from fossil fuels. By implementing CCUS in hydrocarbon fields, incremental oil recovery gained from CO_2 injection may be an incentive to carbon storage.

1.2.1 CO_2 EOR

Enhanced oil recovery by CO_2 injection has been commercially applied for more than four decades, and today, CO_2 EOR is responsible for 5% of the total oil production in the U.S. (Enick and Olsen, 2012). The mature Permian Basin covers southeast New Mexico and western Texas and has been a major target for CO_2 injection under miscible conditions since the early 1970's. The availability of inexpensive, natural CO_2 sources, extensive pipeline infrastructure, favorable reservoir conditions, and relatively high oil prices make CO_2 injection attractive in the U.S. The lack of developed pipeline infrastructure and natural CO_2 sources, combined with off-shore related challenges have so far impeded CO_2 injection in Europe, but the potential for CO_2 EOR in the North Sea is great (Lindeberg and Holt, 1994) and currently evaluated.

Incremental oil recovery from CO_2 injection is a proven method (Grigg and Schechter, 1997). However, it takes about 10 Mcf of CO_2 to recover an incremental barrel of oil (Pope, 2011), causing large quantities of effluent CO_2 that must be separated from the hydrocarbons, re-pressurized and re-injected. Depending on the reservoir pressure, CO_2 processes are classified as miscible or

immiscible. Although immiscible carbon floods improve oil recovery, they are not as effective as miscible floods (Lambert et al., 1996, Kulkarni and Rao, 2004). CO_2 promotes oil swelling, reduces oil viscosity, and can vaporize and extract hydrocarbon components between the leading edge of CO_2 and the oil (Skjæveland and Kleppe, 1992). Hydrocarbon components up to C_{30} can be stripped from the oil through multiple contacts, and CO_2 has the ability to achieve miscibility with oil at relatively low pressures. For most reservoir conditions, liquid or supercritical CO_2 is less prone to viscous instabilities and gravity override compared to other solvents such as nitrogen and methane. Molecular diffusion of CO_2 through water barriers may cause swelling of the oil phase and subsequent mobilization of stagnant oil by evaporation into the flowing gas (Skjæveland and Kleppe, 1992). Thus, CO_2 is less hampered by water shielding effects compared to less water-soluble gases.

CO_2 is an efficient EOR agent in homogenous reservoirs containing light and medium oil, due to the aforementioned properties resulting in excellent microscopic displacement efficiency. In stratified and fractured reservoirs, however, injected CO_2 may cause channeling and bypass large oil zones, and matrix oil is recovered primarily by gravity and molecular diffusion. In such systems, the macroscopic sweep efficiency of CO_2 injection is greatly reduced and the need for mobility control is evident. EOR methods aiming to improve vertical and areal sweep are discussed in section 1.3.

1.2.2 CO_2 Storage and Trapping Mechanisms

Enhanced oil recovery to meet the global energy demand and curbed anthropogenic climate changes are the potential benefits from combining CO_2 for storage and EOR. Hydrocarbon reservoirs are important targets for carbon sequestration due to their integrity against gas escape (Oldenburg et al., 2001). In order to reduce emissions of environmental hazardous gases to the

atmosphere, very high CO_2 retention rates are needed in the migration flow path (Benson and Cole, 2008).

Trapping mechanisms to retain and permanently sequester injected CO_2 in deep sedimentary formations are structural trapping, mineral reaction, fluid dissolution, and capillary trapping. Structural trapping occurs at the onset of the CO_2 injection, whereas mineral trapping (solid state CO_2), considered the most secure trapping mechanism, requires a considerable amount of time due to slow geochemical reaction rates (Gunter et al., 1997). CO_2 is displaced from the injection well by viscous forces and advances to the top of the formation due to gravity segregation. Advancement of CO_2 and water within the formation result in capillary entrapment of CO_2 in the pore space. CO_2 can be trapped as clusters and as individual ganglia (Chaudhary et al., 2013), and capillary entrapment of non-wetting phase by chase water is considered a rapid and efficient way to ensure safe CO_2 storage (Qi et al., 2009).

When the CO_2 plume is immobilized by a stratigraphic feature, e.g. an impermeable anticline, CO_2 diffusion from the gas cap into the water column located below leads to dissolution trapping. CO_2 saturated water is denser than unsaturated formation water, and density gradients may induce vertical convectional currents depending on fluid and reservoir properties. If so, unsaturated formation water will be transported to the gas-water contact, and this process will increase the contribution from dissolution trapping and increase the total storage capacity of the formation (Lindeberg and Wessel-Berg, 1997).

The contribution from, and the relative importance of, the aforementioned trapping mechanisms change over time as CO_2 advances and reacts with reservoir fluids and minerals (Benson and Cole, 2008). Capillary trapping has emerged as one of the dominant mechanisms for long-term carbon storage

(Taku Ide et al., 2007, Rosenbauer and Thomas, 2010) with a substantial amount of entrapped CO_2 reported in core-scale experiments (Iglauer et al., 2011, Pentland et al., 2011). In this thesis, CO_2 trapped by dissolution and capillary forces are evaluated.

1.3 Improving Macroscopic Sweep Efficiency

The macroscopic sweep can be enhanced by altering the mobility ratio between displaced and displacing fluid. For instance, polymer flooding increases the viscosity of injected water and can stabilize the displacement front. In unconventional reservoirs featuring large permeability contrasts, polymer gel can be applied to induce near-wellbore conformance control by plugging high permeable zones. Other methods to improve the macroscopic sweep efficiency are gas mobility control and wettability reversal in oil-wet or weakly water-wet reservoirs.

1.3.1 Water-Alternating-Gas

The method of water-alternating-gas (WAG) was proposed by Caudle and Dyes (1958) and aimed at improving gas flood conformance. WAG is the most widely practiced profile control method in the oil reservoirs today (Kulkarni and Rao, 2004), and based on total enhanced production and number of field applications, WAG appears to be the most successful EOR technology in the North Sea (Teigland and Kleppe, 2006).

Alternating water and gas injection in the reservoir results in a dispersed flow zone and reduced gravity segregation. WAG can potentially increase the microscopic displacement efficiency and reduce the residual oil zone compared to conventional waterflooding. Important design parameters for WAG include rock and fluid characteristics, well pattern, composition of injection gas, WAG ratio, slug size, tapering, and three phase relative permeability effects.

Kulkarni and Rao (2004) reported, based on oil recovery from homogenous Berea cores, that continuous gas injection (CGI) using CO_2 appeared to be better than water-alternating-CO_2 injection. However, when implementing unit of pore volume of CO_2 injected, the WAG process out-performed CGI. Coreflooding results demonstrated that the optimum mode of tertiary injection was a sequence of CGI followed by WAG.

1.3.2 Foam Injection

Foam is a metastable dispersion of gas within a continuous liquid phase where individual gas bubbles are separated by surfactant-stabilized lamellae. Lamellae are created in porous media by snap-off, lamella division or leave-behind (Roof, 1970, Mast, 1972). Snap-off and lamella division creates "strong" foam in terms of separate gas bubbles above a critical capillary number (Ransohoff and Radke, 1988), whereas leave-behind forms lamellae oriented parallel to flow direction with only moderate effect on flow resistance and the injected gas remains as a continuous phase. Foam generation benefits from lower capillary pressure, whereas high capillary pressure causes foam collapse (Khatib et al., 1988, Shan and Rossen, 2004).

Foam impedes the flow of gas in porous media by increasing the apparent gas viscosity (Hirasaki and Lawson, 1985), potentially resulting in enhanced oil recovery through improved macroscopic sweep efficiency. Foam is implemented in the reservoir primarily as mobility control to suppress fingering and gravity override, or as conformance control to block highly permeable thief-zones (Enick and Olsen, 2012). Depending on the application, foam is pre-generated or *in situ* generated by co-injection or by surfactant-alternating-gas (SAG) injection. Foam injection strategy is affected by reservoir pressure, permeability, and foam propagation distance (Turta and Singhal, 2002).

Foam is a proven gas mobility control method in fields (Blaker et al., 2002, Hirasaki et al., 2011, Enick and Olsen, 2012) and in numerous studies (Bernard and Holm, 1964, Holm, 1968, Rossen, 1996, Schramm, 1994, Llave et al., 1990, Lawson and Reisberg, 1980). More recently, foam has been suggested as a gas diversion agent in stratified systems (Bertin et al., 1999, Tanzil et al., 2002, Nguyen et al., 2003, Siddiqui et al., 2003, Li et al., 2010, Li et al., 2011, Conn et al., 2014) and in fractures and fracture networks (Kovscek et al., 1995, Yan et al., 2006, Fjelde et al., 2008, Buchgraber et al., 2012b, Haugen et al., 2012).

Nguyen et al. (2003) demonstrated gas diversion in a layered system, and found that foam penetration depth in the low permeable layer increased when capillary cross-flow was allowed, even if the layers were parallel to the main flow direction. Li et al. (2010) reported enhanced vertical sweep in a two-dimensional stratified sandpack with a 19:1 permeability contrast with SAG compared to conventional waterflood. At such sudden increase in permeability, snap-off is an important mechanism for foam generation (Falls et al., 1988, Rossen, 1999, Tanzil et al., 2002).

Kovscek et al. (1995) observed bulk two-dimensional foam in fractures and that alteration in foam bubble shape occurred near gas fractional flow of 0.91, coinciding with maximum flow resistance. Yan et al. (2006) reported that foam texture, i.e. number of lamellae per unit length, largely controlled the foam viscosity in smooth uniform fractures. Resistance to flow increased with greater gas fractional flow and larger aperture thickness.

1.3.3 Low Salinity Waterflooding

Incremental oil recovery from low salinity waterflooding (LSW) has been demonstrated in field tests (Webb et al., 2004, McGuire et al., 2005, Lager et al., 2008, Seccombe et al., 2010) and in laboratory studies (Tang and Morrow, 1997, Tang and Morrow, 1999). LSW effects are normally reported during water

injections with ionic strengths of about 5000 ppm or less (Morrow and Buckley, 2011). The threshold value is a balance between EOR effects and prevention of formation damage, e.g. swelling (Romanuka et al., 2012).

The main cause of LSW resulting in additional oil recovery beyond conventional waterflooding is wettability alteration towards more water-wet rock surfaces. This will generally improve the recovery of a waterflood (Anderson, 1987). However, a consistent mechanistic explanation to the observed wettability change has not yet emerged. Suggested mechanisms include fines migration, expansion of electrical double-layer, "salt-in" effect, pH alteration, mineral dissolution, saponification, osmotic pressure, and multi-component ion exchange. Depending on the crude oil-brine-rock (COBR) properties, one or a combination of the aforementioned mechanisms may be valid.

The vast majority of successful LSW experiments reported in the literature have been conducted in sandstone porous media. Carbonate surfaces are positively charged and contain less clay compared to sandstone, thus, the prevailing mechanisms during LSW in carbonates are not necessarily the same as reported in sandstones. Additional oil recovery and wettability alterations from LSW in rocks with insignificant clay content have been reported (Webb et al., 2005, Pu et al., 2010, Romanuka et al., 2012). Improved recovery on pure calcite surfaces often require modification of injected water by adding or increasing the concentration of surface interaction ions such as sulfate, phosphate, borate, magnesium or calcium (Austad et al., 2005, Gupta et al., 2011). Sulfate in the imbibing brine increased oil recovery in chalk and limestone rock materials during spontaneous imbibition at elevated temperature (Strand et al., 2008, Fernø et al., 2011). Reduction in the contact angle between crude oil, brine and limestone surfaces (Almehaideb et al., 2004), and enhanced oil recovery by surface charge alteration and microscopic anhydrite dissolution (Yousef et al., 2011) are other effects reported during LSW in carbonates.

In this thesis, the potential for incremental oil recovery during secondary and tertiary LSW in carbonates with insignificant clay and anhydrite content is studied. The results are presented in section 2.4.

1.4 Imaging Techniques

Imaging techniques enabling *in situ* visualization of fluid flow in porous media are vital tools to characterize flow propagation and rock features in opaque systems. Common non-invasive, non-perturbing techniques utilized to obtain flow dynamics within standard cores include attenuation methods; X-ray and X-ray computed tomography (CT), and explicit methods; nuclear tracer imaging (NTI), magnetic resonance imaging (MRI) and positron emission tomography (PET). This section describes supplementary imaging techniques used in this thesis to visualize and quantify fluid dynamics in pores, cores and larger blocks.

1.4.1 Core-Scale Imaging: PET/CT

The method of positron emission tomography (PET), pioneered in the field of medicine and frequently used as a clinical diagnostic tool, has occasionally been used in non-medical applications. Hoff et al. (1996) measured water diffusion through porous construction materials, Degueldre et al. (1996) determined pathway morphology in crystalline rock, Maguire et al. (1997) characterized large rock samples, and Khalili et al. (1998) visualized flow in porous sediments, all using the method of positron emission tomography. Haugan (2000) constructed a low-cost 2D PET system and successfully imaged fingering inside porous media by labeling the water phase with ^{22}Na tracers. Ogilvie et al. (2001) used PET to monitor fluid flow in a sandstone core containing deformation bands, and the authors were able to directly visualize the influence of these discontinuities as potential barriers to fluid flow. More recently, PET has visualized and partly quantified fluid propagation through geomaterials (Kulenkampff' et al., 2008), imaged flow dynamics in porous columns (Boutchko

et al., 2012), qualitatively validated numerical models (Dechsiri et al., 2005, Boutchko et al., 2012), and imaged fluid mobility in naturally fractured shale cores (van Heerden et al., 2013).

Combined PET/CT imaging has to our knowledge not been previously reported in petrophysical research. We image fluid dynamics in porous media by obtaining 4D information from the explicit method (PET) and the attenuation method (CT) sequentially in the same session.

Detection of annihilation gamma ray pairs occurs continuously throughout a PET experiment. Time intervals are determined post-process and can be optimized with respect to studied displacement mechanism. In positron decay, a positron is emitted from the nucleus accompanied by an electron to balance atomic charge. The positron loses kinetic energy as it interacts with the surroundings, and at near-zero momentum, the positron combines with an electron and annihilates at a finite distance outside the radioactive nucleus. The electromagnetic radiation is in the form of two photons of 511 keV which corresponds to the rest-mass energy of each of the particles. The photons are emitted at 180° to conserve momentum and the electromagnetic radiation is detected in PET only if the photon pair is within the coincidence window and the line-of-response (LOR) acceptance angle (Bailey et al., 2005). From the obtained information, the distribution of radionuclides within the object can be reconstructed.

Spatial fluid saturations are calculated from the linear relationship between the number of disintegrations and the saturation of the labeled fluid, described as

$$S_{x,y,z} = \frac{I_{x,y,z}}{A_{x,y,z}} \quad (1)$$

where S is the saturation of the labeled phase at location (x,y,z), I is the time-averaged radiation intensity at location (x,y,z) and A is the time-averaged

intensity value of 100% phase saturation at location (x,y,z). The recorded number of disintegrations is decay corrected and attenuation corrected for spatial density variations within the field of view in the combined PET/CT system. Voxel resolution is 0.6 mm^3 and 2.0 mm^3 for respectively CT and PET in the setup used in this thesis.

CT measures the x-ray attenuation, a function of material density and thickness, beam energy, and effective atomic number, in the system to create density images of both the core and the fluid within. In order to quantify time-averaged phase distributions in a standalone CT, the following definition can be used (Ikeda et al., 1983):

$$\varepsilon_{ij,2} = \frac{CT_{ij} - CT_{ij,1}}{CT_{ij,2} - CT_{ij,1}} \quad (2)$$

where ε_{ij} is the time-averaged phase fraction of phase 2 at location (i,j), CT_{ij} is the time-averaged CT value at location (i,j), and $CT_{ij,1}$ and $CT_{ij,2}$ are the time-averaged CT values of 100% phase 1 saturation and 100% phase 2 saturation at location (i,j), respectively, both obtained through CT reference scans (Heindel, 2011). In CT reconstruction, the magnitude of attenuation occurring within each pixel or voxel is calculated and the effective attenuation coefficient usually relates linearly to CT values. Commercial CT systems typically use an international CT value scale named the Hounsfield Scale, defined as:

$$H = \frac{(\mu - \mu_{water})}{\mu_{water}} x1000 \quad (3)$$

where H is the Hounsfield unit and μ_{water} is the attenuation coefficient of water.

Photons interact with matter by different mechanisms depending on the radiation energy. At low energies (<100 keV), interactions by the photoelectric effect are dominant and here the photon interacts with an orbital electron in an

atom and transfer all of its energy to the electron. The ejected electron from this process is known as a photoelectron. This phenomenon is important in CT scans, but has little impact in PET. At annihilation radiation (511 keV), interactions between photons and electrons occurs by Compton scattering. Here, the incoming photon transfer part of its energy to a loosely bound atomic electron and the photon is deflected through an angle proportional to the amount of energy lost to the recoil electron (Bailey et al., 2005). In the PET/CT setup, correction factors derived from CT scans (~100 keV) are scaled to the 511 keV PET energy by applying a hybrid scaling algorithm (Kinahan et al., 1998).

1.4.2 Pore-Scale Imaging: Microfluidics

The concept of studying pore-level fluid dynamics in two-dimensional micromodels has been around for decades. The use of micromodels allow fluid interfaces to be directly visualized and different mechanisms causing similar behavior on core-scale can be distinguished and identified at the pore-scale. Micromodel applications include processes related to CO_2 storage and trapping (Kim et al., 2012, Soroush et al., 2014), formation and dissociation of hydrates (Tohidi et al., 2001), polymer rheology (Perrin et al., 2006), microbial improved oil recovery (Shabani Afrapoli et al., 2011), matrix-fracture transfer mechanisms (Rangel-German and Kovscek, 2006), and foam flow (Owete and Brigham, 1987). An overview of earlier micromodel studies is summarized in Buckley (1991).

The first micromodels were etched glass models with uniform pore geometry (Mattax and Kyte, 1961, Davis and Jones, 1968). Drawbacks with the earlier models in glass were concave-shaped pore walls, enlarged pore throats and pore bodies, and low coordination numbers. Improved etching techniques in silicon wafer materials led to rectangular pore cross-sections and representation of small-scale pore features. Hornbrook et al. (1991) developed a silicon model based on pore geometry from Berea sandstone. Today's micromodels made from silicon wafer bonded to a glass plate yield rough-walled, complex pore networks

with a 1:1 representation of grain size and aspect ratios. This provides a realistic magnitude of the Peclet number and capillary forces present in the microfluidic system. The models are naturally water-wet due to a film of silicon dioxide coating the surfaces as a result of the bonding process. A detailed etched-silicon micromodel fabrication procedure is described elsewhere (Buchgraber et al., 2012a).

Figure 1 shows etching characteristics (top left), scanning electron microscope (SEM) image of rough, vertical pore walls (top right), and depth profiles (bottom) in an etched-silicon micromodel based on a Berea sandstone thin-section. Typical networks have more than $3.5x10^5$ pores distributed over a 5x5 cm^2 etched pore area, with a constant etching depth of 25 μm (Kovscek et al., 2007). Grain size ranges from 10 μm to 215 μm, and the coordination number varies between 1-5. The dimension of the pore network in the micromodel appears to meet the representative elementary volume (REV) scaling requirements in 2D (Dullien, 1991).

The microfluidic system used in this thesis includes etched-silicon micromodels, syringe injection pump, high-resolution camera and an inverted microscope to document pore-level fluid dynamics. The inverted microscope was fitted with four objective lenses, neutral density filters, and green and blue fluorescence filter cubes with individual exciter, emitter and dichroic beamsplitter. This allowed specific fluids to be dyed with fluorescent for improved phase identification. A detailed description of the microfluidic system is given in 4 - Appendix.

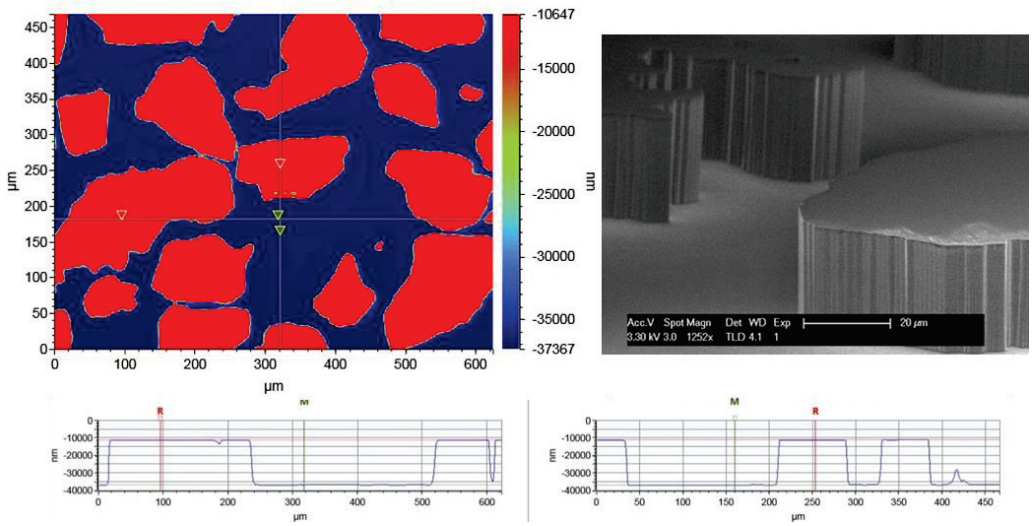

Figure 1 - Left: Pore etching depth is 25 µm throughout the pore network. Right: Scanning Electron Microscope (SEM) image showing the sharp corners and rough walls in the micromodel. Bottom: 1D depth profiles showing etching depth and pore walls etched perpendicular to the flat silicon wafer floor (Pharmafluidics, 2013)

2. Results and Discussion

The main results from the six scientific papers included in this thesis are presented and discussed here. The first part of this chapter is devoted to the novel imaging approach enabling explicit fluid detection in porous media. **Paper 1** and **2** demonstrate the benefits from combined PET/CT imaging of fluid dynamics and structural properties in conventional and unconventional formations. By detecting explicit signals from the water phase (**Paper 1**) and the CO_2 phase (**Paper 2**), fluid saturations were quantified and flow pattern visualized in superimposed 3D images. The second part of this chapter revolves around CO_2 utilization and storage, and methods of enhancing oil recovery by improving the macroscopic sweep efficiency. **Paper 1-3** describe CO_2 distribution and propagation within heterogeneous porous rocks and micromodels in processes related to CCUS. **Paper 4-6** present methods of enhancing the contact area between displacing and displaced fluid in porous media and fracture networks.

2.1 PET/CT: A Novel Imaging Approach

Benefits and important scientific contributions from conducting PET/CT imaging of fluid flow in porous rocks are discussed here. The combined imaging, in a single gantry, obtained data from both the explicit method and the attenuation method sequentially in the same session.

2.1.1 Flow Characterization

A selection of PET compatible radionuclides exists in terms of half-life and mixing properties and both explicitly water (**Paper 1**) and CO_2 (**Paper 2**) were investigated to determine distribution and flow of these phases during oil recovery and CO_2 storage. A major advantage with PET is that temporal resolution is defined in post-processing and can therefore be optimized to capture different displacement processes in the same experiment. Table 1 lists radionuclides used in this thesis for explicit phase identification in porous

media. Due to the relatively short half-life, ^{11}C nuclides were generated in a particle accelerator located on-site.

Table 1 – Tracers in PET/CT

Radionucleus	Phase labeled	Photon energy	Half time	Initial activity
^{22}Na	Water	511, 1275 keV	2.6 years	0.037 GBq
^{11}C	CO_2	511 keV	20.4 min	3 GBq

Whereas attenuation methods primarily yield structural information and rely on density differences to visualize dynamic processes, explicit imaging techniques measure fluids only. The advantage of combining CT imaging (porosity distribution, flow conduits and flow barriers) with explicit PET imaging of fluid dynamics was demonstrated in **Paper 1** and **Paper 2**. The results imply that PET/CT can be used to differentiate fingering and instabilities caused by unfavorable mobility ratios from flow instabilities caused by rock discontinuities.

2.1.2 Sample Size and REV

Representative elementary volume (REV) defines the smallest volume where a measured property, e.g. porosity and permeability, gives an accurate representation of the whole system. REV in porous media is strongly coupled to rock heterogeneity, thus complex carbonates tend to require greater REV than more homogenous sandstone rocks. Determining the REV size is not straightforward as it depends on the nature of the specific material, the parameter studied, and micro-scale parameters that impact macro-scale properties (Al-Raoush and Papadopoulos, 2010).

In **Paper 1**, the effect of sample size on fluid flow in carbonates was investigated, and a standard core system was compared to a 550% larger block system. Both systems are larger than the REV for this rock type, as porosity and absolute

permeability values are similar. The PET/CT setup benefits from a bore diameter of 700 mm and axial field of view of 169 mm in the PET detector array, allowing large samples beyond standard core sizes to be imaged. Results showed that sample size affected residual saturations, initial water distribution, and macroscopic sweep efficiency in carbonates. Growing viscous fingers were observed in the standard core system, but did not develop to form an unstable front due to size constrains. In contrast, the block system allowed front instabilities to develop with less influence from system boundaries due to increased size. Thus, the REV size to capture flow appears to exceed the standard core size when evaluating macroscopic properties such as sweep and recovery in the carbonate rock material.

2.1.3 Microporosity and Tight Formations

PET offers excellent signal-to-noise ratio (SNR) compared to conventional attenuation methods. Where CT needs a relatively large volume of pore space occupied with fluids to perform saturation rendering, PET is highly sensitive and requires a tracer activity as low as 10^{-12} mol/l (Kulenkampff' et al., 2008). This is beneficial in samples featuring micropores and in tight shale where the matrix porosity can range from 0.5% to 9% (Lee et al., 2011). Attenuation methods struggle to provide accurate representation of fluid distribution within such unconventional media (Tovar et al., 2014) due to small variations in density. An explicit method such as PET, however, measures the electromagnetic radiation only, not the surrounding rock, and provides substantial SNR in order to reconstruct the fluid distribution in tight formations.

An example is given in **Paper 2**, where CO_2 propagation in a layered reservoir shale core was imaged using decoupled PET/CT. Figure 2 shows an image series of a) shale core obtained from CT, b) high density shear bands within the shale, c) CO_2 flow from PET, and d) superimposed image containing fluid flow (PET) and rock discontinuities (CT). It is evident that the high density shear bands

identified from CT imaging affects the CO_2 propagation pattern and macroscopic sweep within the pore network. Also, the 3D rendering provides evidence of viscous flow of CO_2 in tight non-fractured, reservoir shale. This may create opportunities for CO_2 EOR in unconventional formations without fracturing the media, but also a cause for concern regarding carbon sequestration and the role of shale as a structural trap to prevent gas escape to the atmosphere.

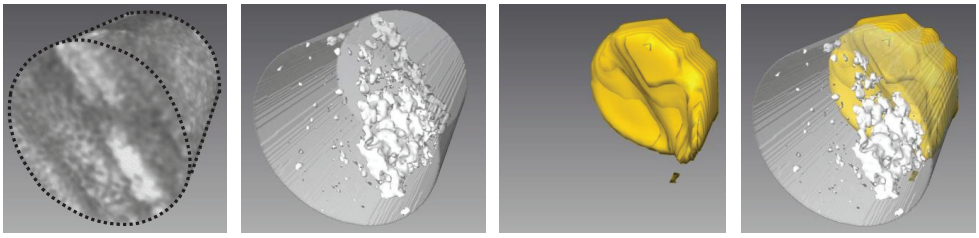

a) b) c) d)

Figure 2 – 3D rendering of a) shale core from CT, b) deformation bands within the core, c) PET image of CO_2 only, and d) superimposed image of fluid distribution and rock discontinuities

2.2 CO_2 Injection

This section describes CO_2 distribution and propagation in core samples (**Paper 1** and **Paper 2**) and in single pores (**Paper 3**). Oil recovery by CO_2 injection and processes related to CO_2 storage in sedimentary formations are discussed.

2.2.1 Determining CO_2 Storage Capacity

A successful CO_2 sequestration project depends upon high storage capacity and high retention rate of CO_2 in the porous medium. The measured storage capacity in a laboratory experiment depends on capillary number, fluid properties and rock material. CO_2 storage capacity in a tilted Bentheim core resembling a dipping reservoir layer was investigated in **Paper 1**. Liquid CO_2 was injected at capillary number of $7.6*10^{-10}$ into the fully water saturated porous rock. Fluids were not equilibrated prior to injection and added a dissolution effect to the

otherwise immiscible displacement. Determining the quantity of explicitly labeled water displaced by CO_2 provided estimates of the CO_2 storage capacity.

Figure 3 shows CO_2 propagating upwards in the core sample where viscous fingers developed with preferred CO_2 flow paths along the edges of the cylindrical core plug, whereas water remained primarily in the center of the rock. Gravitational forces amplified instabilities and further segregated injected CO_2 from the water phase, resulting in early CO_2 breakthrough after 0.4 PV injected and poor sweep efficiency near the outlet side of the tilted core sample. Another 2.1 pore volumes of CO_2 were injected without any significant changes in saturation distribution. Upwards $LqCO_2$ injection in the Bentheim sandstone resulted in an overall storage capacity of 23% in the representative pore space. Similar results have been reported in pore-scale (Chaudhary et al., 2013) and core-scale (Krevor et al., 2012) experiments.

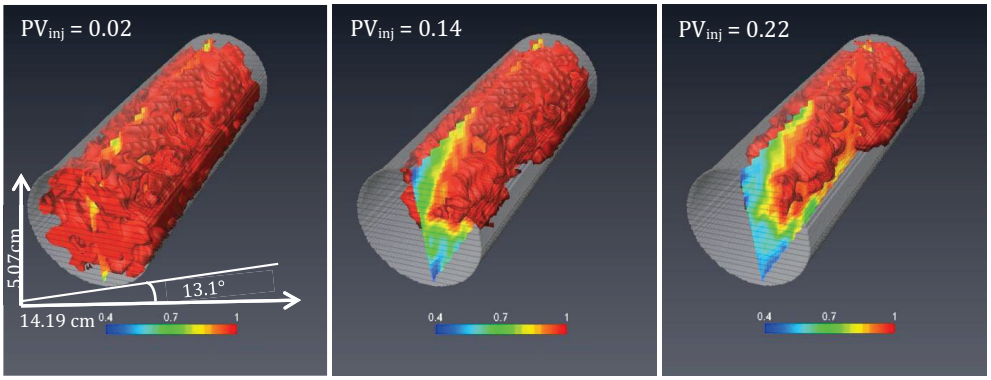

Figure 3 – CO_2 migration at selected time steps in a tilted Bentheim core. Warm colors indicate large quantities of water labeled with sodium-22 nuclides. CO_2 was injected upwards at a constant flow rate of 2.5 cm^3/h

2.2.2 Trapping Mechanisms

In **Paper 2**, capillary entrapment of CO_2 was quantified in Bentheim core samples using combined PET/CT imaging. Following the CO_2 injection during

primary drainage, water was injected at constant flow rate of 0.5 cm^3/min. Relative changes in CO_2 fractions over the core length was quantified from the explicitly labeled gas phase using PET. Results indicated that on average 62% of CO_2 was trapped within the porous rock after 0.60 PV of water injected. Less CO_2 was trapped in the vicinity of the inlet side (X_D=0.0–0.3) compared to the core average due to a dissolution effect. The fractional, residual CO_2 saturation was uniformly distributed from core length X_D=0.3–1.0. In this region, about 66% of the injected CO_2 was retained by capillary forces primarily and corroborates similar results on capillary entrapment of CO_2 in sandstone (Iglauer et al., 2011, Akbarabadi and Piri, 2013). In order to further describe mechanisms associated with capillary trapping and dissolution effects, experiments conducted on the micro-scale were needed.

Pore-level CO_2 trapping was qualitatively studied in a water-CO_2 imbibition process in **Paper 3**. Here, injected water was dyed with fluorescent in order to improve fluid identification in the water-wet micromodel. Methods of capillary entrapment of CO_2 by water were monitored using an inverted microscope as unsaturated water was injected at constant flow rate into a CO_2 saturated micromodel. Water fingers developed in the matrix and advanced perpendicular and in the opposite direction of the bulk flow. Instabilities were manifested by a capillary dominated flow behavior. CO_2 was trapped in single pores by film thickening leading to snap-off, and trapped as a result of bypassing of several pores by Haines jumps due to capillary contrasts. Clusters of CO_2 were trapped in larger pores when water fingers advanced in smaller pores and merged, as shown in Figure 4. Retained CO_2 was also documented in pores with low coordination number (dead-end pores), and the residual phase was poorly connected throughout the network.

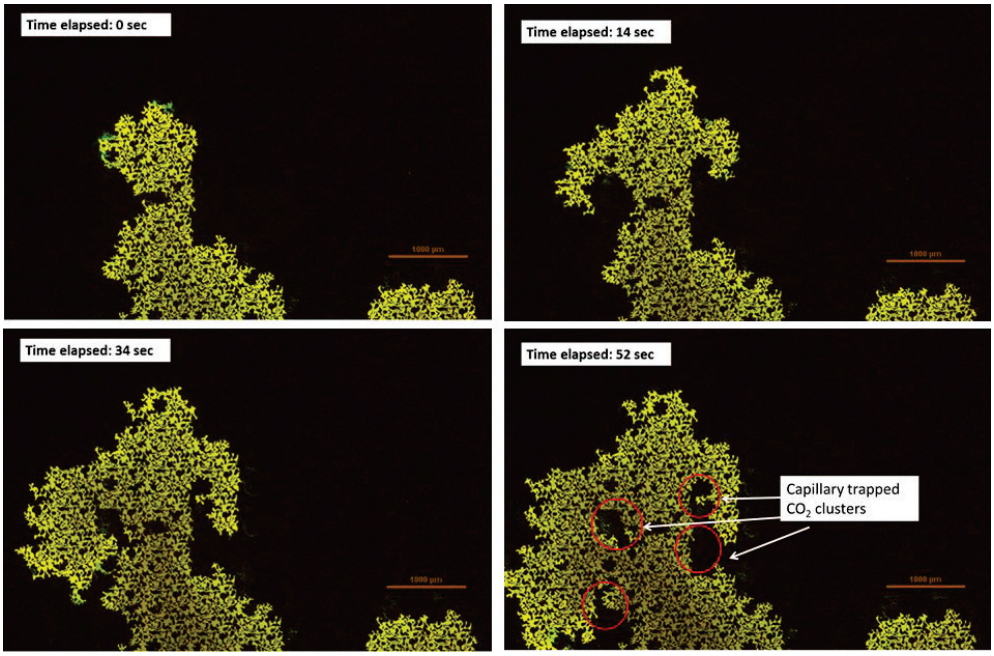

Figure 4 – Pore-level capillary trapping of CO_2 (black) by water (yellow). Bulk flow direction is from bottom to top in the images and scale bar in the right corner is 1000 µm

Discontinuous CO_2 was not mobilized in the porous network but rather dissolved in contact with unsaturated water. Buchgraber et al. (2012c) reported that shrinking and complete dissolution of gas bubbles only occurred after the continuous gas phase was isolated and made immobile by capillary trapping, consistent with observations in **Paper 3**.

2.2.3 CO_2 Injection for EOR

In **Paper 3**, CO_2 was injected at constant pressure in a micromodel partially filled with oil and water similar to a tertiary oil recovery scenario. Oil was the intermediate wetting phase, and a spreading configuration was observed on the pore-scale where a stable oil layer able to conduct flow separated connate water from the non-wetting gas. The spreading oil layer was a consequence of interfacial tensions as well as the geometry of the cross-sectional flow area in the pore network. A positive spreading coefficient for oil has also been reported

in glass micromodels at reservoir conditions (Robin et al., 2012). Injected CO_2 propagated in preferred flow paths mainly through oil-filled pores resulting in an efficient oil production at pore-scale, even at high initial water saturation. The nature of the spreading layer caused oil to maintain hydraulic conductivity during CO_2 injection, which further decreased the residual oil saturation although the initial piston displacement of oil by CO_2 occurred much faster than drainage of the spreading oil layer. Connate water was mobilized through double drainage, and multiple displacement events occurred frequently in the porous media. As a consequence, local fluid distribution changed rapidly and gas flow paths shifted accordingly, resulting in trapped CO_2 bubbles associated with the process of breaking and forming of gas channels.

Oil production by continuous CO_2 injection was scaled up in **Paper 2**. Here, CO_2 propagation in a fractured Bentheim core sample was studied in the PET/CT setup emphasizing CO_2 diffusion as a recovery mechanism. Molecular diffusion is often ignored in conventional reservoirs, but plays an important role in fractured systems with insignificant contribution from viscous forces (Hoteit and Firoozabadi, 2009). The Bentheim core was cut longitudinal and a fracture aperture of 1 mm throughout the core length was controlled by a POM (Polyoxymethylene) spacer. Injected CO_2 advanced primarily in the open fracture, causing gas channeling and sudden breakthrough. After gas breakthrough, increase in CO_2 intensity in adjacent pores was ascribed to molecular diffusion of CO_2 into the matrix and subsequent mobilization of stagnant oil. A gravity effect was present in the fracture where oil was overlying CO_2 throughout the experiment.

Figure 5 shows accumulated CO_2 distribution within the fractured rock at four different time steps. Even though the vertical fracture equals the core diameter, CO_2 is only observed in the lower part of the rock. The CO_2 saturation in the fracture stabilized after 11 minutes, but the mass transfer between the gas and

oil was ongoing throughout the experiment (171 min). As the saturation of CO_2 increased in the matrix proximal to the fracture, reduced driving forces were observed slowing the progress. Diffusive CO_2 reached the transverse core boundaries after 31 minutes. An extended and symmetric CO_2 distribution was obtained in the lower part of the rock, confirming molecular diffusion as the main driving mechanism. However, the total macroscopic sweep in the entire core was limited. In order to further improve the CO_2 areal and vertical sweep efficiency in fractured rocks, mobility control and gas diversion agents could be applied. This is further discussed in section 2.3.

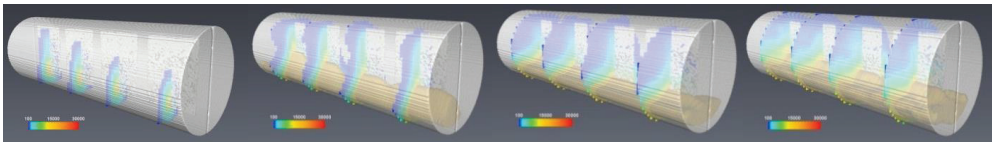

Time: 1 min Time: 21 min Time: 71 min Time: 171 min

Figure 5 – CO_2 displacing oil in a fractured rock imaged by PET/CT. An isosurface (brown color) shows areas with high accumulation of CO_2 (threshold=1 MBq/cm^3) in the porous media. Four transverse orthoslices are included to show radial CO_2 distribution within each sector.

2.3 Foam Injection

4D imaging data from **Paper 1** and **2** revealed instabilities during pure CO_2 injection such as viscous fingering and gravity override, causing early gas breakthrough in heterogeneous systems. **Paper 4** and **5** propose foam injection as a method to impair the mobility of injected gas and increase the sweep efficiency in stratified systems and fracture networks. Foam's ability to divert gas from high permeable layers to low permeable layers highly depends on foam texture and the foam generation process. Therefore, both pore-level events describing the forming and breaking of foam and macroscopic effects such as viscous pressure drop and sweep efficiency have been investigated in **Paper 4** and **Paper 5**.

2.3.1 Foam Generation and Texture

Foam is generated by three distinct mechanisms; snap-off, lamella division and leave-behind. Foam generation is affected by pore topological properties, wetting content, capillary suction pressure, surfactant formula, gas fractional flow and flow rate. Pore-level foam generation mechanisms were investigated in **Paper 5,** where foam was injected at various gas fractions in water and oil saturated micromodels. Here, rectilinear snap-off and snap-off at permeability discontinuities were identified as important mechanisms for *in situ* foam generation. Foam bubbles created at the exit of the constriction appeared more finely textured with smaller average bubble diameter compared to bubbles created by rectilinear snap-off, consistent with Huh et al. (1989) and Chambers and Radke (1991). Subdivision of foam bubbles at branching pores in the interior of the micromodel was not observed.

In **Paper 4**, foam was successfully generated in rough-walled, calcite fracture networks during SAG and co-injection of gas and surfactant solution. Bubble densities were mapped during co-injection for gas fractions f_g=0.80, f_g=0.90 and f_g=0.95 with constant total flow rate of 3 cm^3/min. Foam bubble size increased with increased gas fraction, consistent with earlier results on foam flow in fractures (Kovscek et al., 1995). This effect may be attributed to thinning of lamella at high gas fractional flow (documented in **Paper 5**), resulting in foam coalescence and merging of smaller bubbles. Furthermore, bubble size was uniformly distributed in the fracture for f_g=0.80, whereas a larger distribution in bubble size existed for greater gas fractions. The bubble shape was polyhedral for all three fractional flows. Bubble shape in porous media (**Paper 5**) was dictated by pore configuration, whereas bubble shape in fractures (**Paper 4**) is deformed according to interfacial tension, and the gas-liquid interfacial curvature varies according to foam quality (Pancharoen et al., 2012).

2.3.2 Flow Resistance in Fractures

The pressure response in a fracture network (**Paper 4**) for different gas fractional flows and total flow rates during co-injection of surfactant solution and gas is presented in Figure 6. The viscous pressure drop increased with increasing gas fractions for total flow rates 1, 3, 5 and 8 cm^3/min. The pressure increase is most prominent between f_g=0.85-0.95. Here, liquids drain from the lamella to the Plateau border due to increased capillary suction-pressure. This resulted in thinning of lamellae and alteration in bubble shape from circular to polyhedral foam accompanied by an increase in flow resistance. The measured pressure gradients peak about f_g=0.95. Other work on foam in fractures reported bubble shape alteration and maximum flow resistance at f_g=0.91 (Kovscek et al., 1995). A sudden drop in differential pressure occurred after f_g=0.95 for all flow rates and is attributed to foam coalescence in the fracture network.

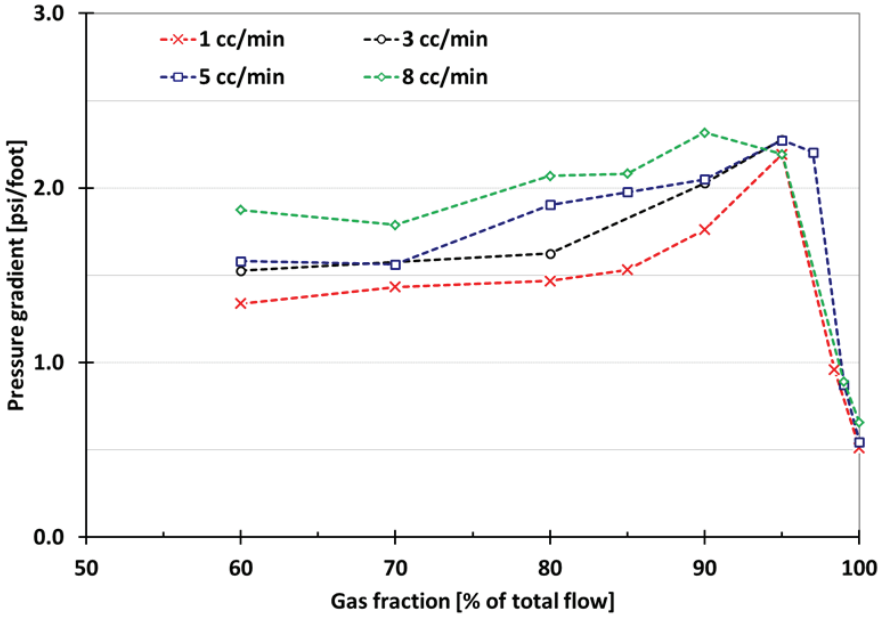

Figure 6 – Pressure gradients versus gas fractions during co-injection of surfactant solution and gas using constant total flow rates of 1, 3, 5 and 8 cm^3/min in a fracture network

Foam rheology in fractures was studied by calculating apparent viscosity during co-injection of gas and surfactant solution. Gas mobility reduction factors spanned from about 200 to 1000 depending on gas fractional flow and total flow rate. The foam generated in rough-walled, calcite fracture network demonstrated a shear-thinning behavior, consistent with other work in smooth-walled systems (Hirasaki and Lawson, 1985, Yan et al., 2006).

2.3.3 Fracture Filling Sequences and Sweep Efficiency

In **Paper 4**, fracture network filling sequences and areal sweep efficiency were evaluated during continuous gas injection (CGI), surfactant-alternating-gas (SAG) and co-injection of gas and surfactant solution (f_g=0.6) at total flow rate of 1 cm^3/min. The fracture network was subdivided into smaller parts and fluid propagation within each sector was monitored. Figure 7 shows local sweep efficiency as a function of normalized network length for CGI, SAG and co-injection at gas breakthrough for CGI. CGI experienced breakthrough after 0.4 fracture volumes (FV) injected. At this time step, SAG was advancing in sector 3 and co-injection had just entered sector 2. Gas breakthrough for SAG and co-injection occurred at respectively 0.60 FV and 0.72 FV. Final sweep efficiency for the three injection strategies was 52.2% (CGI), 61.8% (SAG) and 77.2% (co-injection). The results showed that foam (SAG and co-inj) effectively delayed gas breakthrough and improved sweep efficiency compared to CGI in the fracture network. Furthermore, co-injection of surfactant solution and gas was superior to SAG in five out of six sectors. The flow pattern during co-injection consisted of substantial cross-flow and the injection pattern was less dictated by the large longitudinal fractures compared to SAG and CGI.

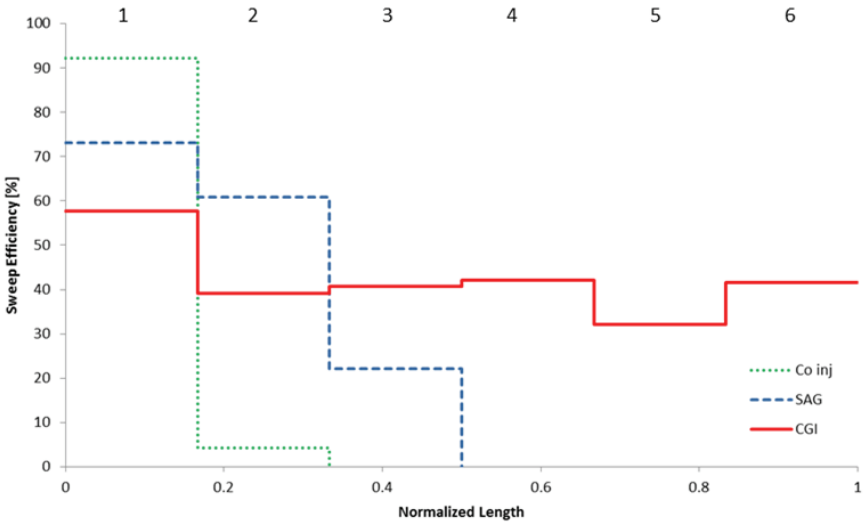

Figure 7 – Comparison of local sweep efficiency at gas breakthrough during CGI (red), SAG (blue) and co-injection (green) in the fracture network subdivided into six sectors

Pore-scale areal sweep efficiency during CGI and foam injection was evaluated in water-wet micromodels in **Paper 5**. Here, pre-generated foam successfully diverted gas from the high permeable fracture to the low permeable matrix. Final sweep efficiency for foam was 87% within matrix field of view. CGI failed to establish a viscous pressure drop high enough to overcome the matrix threshold pressure.

2.4 Low Salinity Waterflooding

Increased sweep in heterogonous and fractured systems by foam injection was presented in **Paper 4** and **5**. Another EOR method in fractured, hydrophobic media is wettability reversal. Spontaneous imbibition controlled by capillary forces is an important recovery mechanism in fractured reservoirs, and the efficiency of capillary imbibition is strongly influenced by reservoir wettability (Zhou et al., 2000). By altering this parameter and establish water-wet rock surfaces during low salinity waterflooding (LSW), water may spontaneously imbibe into unswept areas because the rock threshold pressure is terminated,

and thus improve the areal and vertical sweep efficiency. **Paper 6** describes LSW effects at reservoir conditions in aged carbonates having insignificant clay and anhydrite content. Work in progress on osmotic gradient induced oil recovery in micromodels is also discussed.

2.4.1 Fluid-Fluid Interactions

Interfacial tensions between the reservoir crude oil and brines with varying ionic strength were measured in a pendant drop setup. The visualization cell was filled with brine, and droplets of crude oil were injected through a needle from the bottom of the cell. Interfacial tensions were derived from droplet geometry by applying the Young-Laplace equation. **Paper 6** proved that interfacial tensions between oil and brine decreased with reduced brine salinity. By replacing synthetic brine (TDS=92.47 g/l) with low salinity brines (TDS=18.49 g/l and TDS=1.849 g/l), interfacial tensions were reduced by almost 30%. Similar trends have been reported by others (Okasha and Alshiwaish, 2009, Yousef et al., 2012). This effect will increase the capillary number and may contribute in mobilizing residual oil during LSW if the critical capillary number is exceeded.

2.4.2 Fluid-Rock Interactions

Unsteady-state relative permeability measurements were conducted on three twin plugs. Brines with varying ionic strength were injected at constant flow rate of 0.5 cm^3/min in carbonates initially saturated with crude oil at irreducible water saturation. Fractional flow calculations during oil and water production were obtained from the Johnson-Bossler-Neumann approach. Results demonstrated an increase in oil relative permeability endpoints and decrease in water relative endpoints during LSW compared to high salinity waterflooding (HSW). These observations indicated that the relative permeability curves shifted towards more water-wet characteristics (Craig, 1971) when lowering the ionic strength of injected water. Thus, wettability alterations on the carbonate

surface during LSW were indirectly confirmed by relative permeability measurements.

2.4.3 Incremental Oil Recovery

Secondary and tertiary LSW were conducted at constant injection flow rate and compared to HSW baseline experiment yielding identical boundary conditions. LSW responded in additional oil recovery up to 7.5% OOIP (twin core) in secondary mode and up to 10.2% OOIP (same core) in tertiary recovery mode beyond conventional HSW. These results imply that LSW as an EOR method can, depending on the COBR properties, be implemented on an early stage in less water-wet fields, but also target the numerous mature, watered-out carbonate formations in production worldwide.

2.4.4 Osmotic Gradient

The enhanced oil recovery associated with LSW in **Paper 6** is likely caused by a combination of fluid-fluid and fluid-rock interactions. In addition to wettability alteration, osmosis may lead to incremental oil recovery during LSW. Oil mobilization within single pores was investigated in two-dimensional micromodels with constant wetting preferences. The osmotic gradient was induced by conducting a LSW in the fracture at low flow rate. Pore-level oil mobilization by water diffusion (osmosis) was then monitored in a layered system where viscous forces were absent. An oil layer separated the saline formation water (matrix) from the low salinity water (fracture). A standard experimental procedure is detailed in Appendix 4.3.

Results using mineral oils demonstrated qualitatively pore-scale mobilization of retained oil and counter-current displacement of oil from the matrix into the fracture. Water molecules diffused from the fracture and into the matrix where the oil layer acted as a semi-permeable membrane. As a result, formation water swelled and increased in volume inside the matrix, and oil was subsequently

displaced towards the fracture. Figure 8 shows before and after pictures of water diffusion from fracture towards matrix through a layer of crude oil during LSW without contribution from viscous forces and capillary imbibition. The oil phase (brown color) proximal to the fracture darkened gradually as water migrated through it.

Osmosis has been proposed as a significant driving force for oil movement (Sandengen and Arntzen, 2013), although the process demands a long exposure time as documented here in 2D media at ambient temperature. Thus, the osmotic gradient mechanism may contribute to additional oil recovery in lengthy spontaneous imbibition experiments, however, it is not a dominant mechanism during coreflood LSW as described in **Paper 6**.

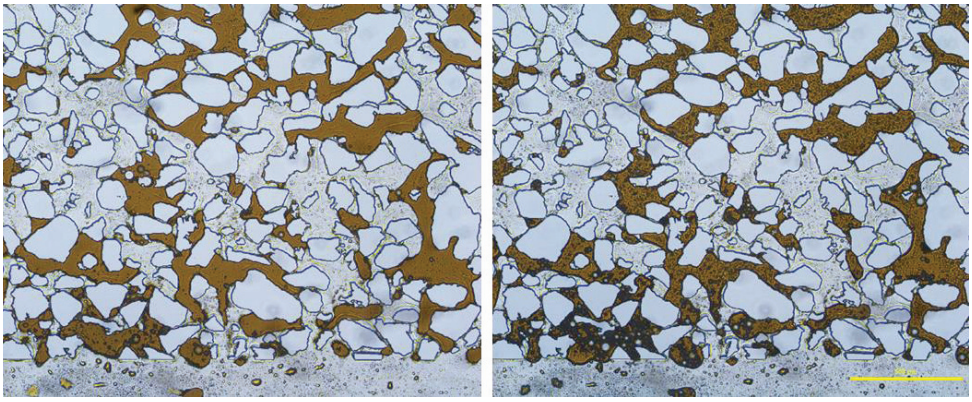

Figure 8 – Before (left) and after (right) transport of LSW from the fracture to the matrix through a layer of crude oil. The time difference between the images is 194 hours and the scale bar in the lower right corner reads 500 µm

3. Conclusions and Perspectives

The main findings in this thesis are summarized and presented here as well as future perspectives regarding the experimental work.

3.1 Conclusions

- A novel approach using positron emission tomography (PET) and computed tomography (CT) was implemented in a series of flow experiments where sample size, porosity, level of heterogeneity and recovery mechanisms varied. Simultaneous decoupled structural rock information (CT) and explicit fluid saturation information (PET) provided a robust imaging technique. Superimposed images identified flow instabilities caused by rock discontinuities in samples from conventional and unconventional formations due to the high sensitivity of PET. The imaging technique offers excellent temporal resolution, and time intervals are defined and optimized in post-processing with respect to studied displacement mechanism
- Continuous CO_2 injection in etched-silicon micromodels displaced oil efficiently due to the presence of a spreading oil layer. However, in larger and more complex structures, CO_2 EOR resulted in poor macroscopic sweep and early gas breakthrough. Molecular diffusion was the dominant oil recovery mechanism in fractured core sample. A large fraction of the injected CO_2 was retained in pores by capillary forces, demonstrating the potential for safe CO_2 sequestration. CO_2 was trapped in single pores and in larger clusters, and the residual phase was poorly connected throughout the pore network
- Foam rheology was studied at pore-scale and in heterogeneous fracture networks. Foam was superior to continuous gas injection (CGI) and water-alternating-gas (WAG) in terms of areal sweep and mobility reduction factor. Co-injection of gas and surfactant solution resulted in higher apparent viscosity and delayed gas breakthrough compared to

surfactant-alternating-gas (SAG). Lamella creation occurred *in situ* in pores and in fractures, and rectilinear snap-off and snap-off at permeability discontinuities were identified as important foam generation mechanisms

- Low salinity waterflooding (LSW) in carbonates resulted in enhanced secondary and tertiary oil recovery. Wettability alteration and interfacial tension reduction between crude oil and water were effects ascribed to LSW. Osmotic pressure was not a dominant oil recovery mechanism during low salinity corefloods

3.2 Future Perspectives

Foam experiments presented in this thesis should be scaled and conducted in heterogeneous and fractured cores and larger blocks, preferably at reservoir conditions. PET/CT would serve as an excellent imaging tool in order to visualize and quantify foam propagation and volumetric sweep efficiency in larger opaque systems. To further optimize fluid flow description in PET/CT, a contrast liquid should be added in the water phase if saturation rendering by CT is needed. Field pilot tests of CO_2 and CO_2-foam injections combined with 4D seismic are currently ongoing in watered-out reservoirs in West Texas, U.S. This collaborating project between international academic institutions and industrial partners was initiated by the reservoir physics group here at the University of Bergen. Reservoir imaging by logging and seismic data are essential in order to monitor *in situ* fluid dynamics. By comprehending pore-, core-, block- and pilot field-scale mobility control data, a thorough prediction of the process in complex reservoirs can be achieved.

Low salinity effects in carbonates are an ongoing experimental study. Incremental oil recovery and indirect wettability alteration by changes in relative permeability were observed in this thesis. A more direct way to determine wettability alteration in carbonates involves contact angle

measurements on a calcite surface before and after LSW. However, it can be challenging making an artificial disc mimicking the mineral surface of the rock sample. X-ray diffraction (XRD) should be used to determine rock mineral composition. To further determine mechanisms involved in LSW, pH measurements of initial and effluent fluids as well as inductively coupled plasma (ICP) analysis could identify fluid-rock interactions.

Pore-scale oil mobilization by osmotic pressure is work in progress. The study has so far investigated the impact of brine salinity, oil composition and thickness of semi-permeable layer on oil recovery in water-wet porous media. Future work on this topic will involve the effects of temperature and wettability on water diffusion in etched-silicon micromodels. Wettability alterations can be induced by flooding the models with crude oil and aged with no initial water saturation (Buchgraber et al., 2012a). Film flow of water along the surfaces in an oil-wet micromodel can be neglected and only water diffusion through the semi-permeable layer contributes in swelling of formation water and subsequent oil mobilization. By comparing water-wet and oil-wet results, the effect of film flow can be determined.

Pore- and core-scale experimental results in this thesis should be compared to numerical simulated outcomes to better validate the experimental findings. When the observed *in situ* fluid flow behavior is captured and implemented in numerical models, upscaling and time-efficient numerical sensitivity studies can be conducted.

Abbreviations

CCUS	Carbon capture utilization and storage
CGI	Continuous gas injection
COBR	Crude oil-brine-rock
CT	Computed tomography
EOR	Enhanced oil recovery
FV	Fracture volume
HSW	High salinity waterflooding
ICP	Inductively coupled plasma
ID	Inside diameter
LOR	Line-of-response
$LqCO_2$	Liquid CO_2
LSW	Low salinity waterflooding
MRI	Magnetic resonance imaging
NTI	Nuclear tracer imaging
OD	Outside diameter
OOIP	Oil originally in place
PET	Positron emission tomography
POM	Polyoxymethylene
PV	Pore volume
REV	Representative elementary volume
SAG	Surfactant-alternating-gas
SEM	Scanning electron microscope
SNR	Signal-to-noise ratio
TDS	Total dissolved solids
WAG	Water-alternating-gas
XRD	X-ray diffraction

Nomenclature

A	Time-averaged radiation intensity at 100% phase saturation
CT_{ij}	Time-averaged CT value at location i,j
f_{g}	Gas fraction
H	Hounsfield unit
I	Time-averaged radiation intensity
S	Saturation
X_{D}	Dimensionless length
$\varepsilon_{i,j}$	Time-averaged phase fraction at location i,j
μ	Attenuation coefficient

Bibliography

AKBARABADI, M. & PIRI, M. 2013. Relative permeability hysteresis and capillary trapping characteristics of supercritical CO2/brine systems: An experimental study at reservoir conditions. *Advances in Water Resources,* 52**,** 190-206.

AL-RAOUSH, R. & PAPADOPOULOS, A. 2010. Representative elementary volume analysis of porous media using X-ray computed tomography. *Powder Technology,* 200**,** 69-77.

ALMEHAIDEB, R. A., GHANNAM, M. T. & ZEKRI, A. Y. 2004. Experimental Investigation of Contact Angles Under Oil-Microbial Solution on Carbonate Rocks. *Petroleum Science and Technology,* 22**,** 423-438.

ANDERSON, W. G. 1987. Wettability Literature Survey - Part 6: The Effects of Wettability on Waterflooding. *Journal of Petroleum Technology***,** 1605-1622.

AUSTAD, T., STRAND, S., HØGNESEN, E. J. & ZHANG, P. 2005. Seawater as IOR Fluid in Fractured Chalk. Society of Petroleum Engineers.

BAILEY, D. L., TOWNSEND, D. W., VALK, P. E. & MAISEY, M. N. 2005. *Positron Emission Tomography: basic science*, Springer.

BENSON, S. M. & COLE, D. R. 2008. CO2 Sequestration in Deep Sedimentary Formations. *Elements,* 4**,** 325-331.

BERNARD, G. G. & HOLM, L. W. 1964. Effect of Foam on Permeability of Porous Media to Gas.

BERTIN, H. J., APAYDIN, O. G., CASTANIER, L. M. & KOVSCEK, A. R. 1999. Foam Flow in Heterogeneous Porous Media: Effect of Cross Flow.

BLAKER, T., AARRA, M. G., SKAUGE, A., RASMUSSEN, L., CELIUS, H. K., MARTINSEN, H. A. & VASSENDEN, F. 2002. Foam for Gas Mobility Control in the Snorre Field: The FAWAG Project.

BOUTCHKO, R., RAYZ, V. L., VANDEHEY, N. T., O'NEIL, J. P., BUDINGER, T. F., NICO, P. S., DRUHAN, J. L., SALONER, D. A., GULLBERG, G. T. & MOSES, W. W. 2012. Imaging and modeling of flow in porous media using clinical nuclear emission tomography systems and computational fluid dynamics. *Journal of Applied Geophysics,* 76**,** 74-81.

BUCHGRABER, M., AL-DOSSARY, M., ROSS, C. M. & KOVSCEK, A. R. 2012a. Creation of a dual-porosity micromodel for pore-level visualization of multiphase flow. *Journal of Petroleum Science and Engineering,* 86–87**,** 27-38.

BUCHGRABER, M., CASTANIER, L. M. & KOVSCEK, A. R. Microvisual Investigation of Foam Flow in Ideal Fractures: Role of Fracture Aperture and Surface Roughness. SPE Annual Technical Conference and Exhibition, 8-10 Oct 2012 2012b San Antonio, TX, US. SPE: Society of Petroleum Engineers.

BUCHGRABER, M., KOVSCEK, A. & CASTANIER, L. 2012c. A Study of Microscale Gas Trapping Using Etched Silicon Micromodels. *Transport in Porous Media,* 95**,** 647-668.

BUCKLEY, J. S. 1991. Multiphase Displacements in Micromodels. *In:* MORROW, N. (ed.) *Interfacial phenomena in petroleum recovery.* Marcel Dekker Inc.

CAUDLE, B. H. & DYES, A. B. 1958. Improving Miscible Displacement by Gas-Water Injection. Society of Petroleum Engineers.

CHAMBERS, K. T. & RADKE, C. J. 1991. Capillary Phenomena in Foam Flow Through Porous Media. *In:* MORROW, N. (ed.) *Interfacial phenomena in petroleum recovery.* Marcel Dekker Inc.

CHAUDHARY, K., BAYANI CARDENAS, M., WOLFE, W. W., MAISANO, J. A., KETCHAM, R. A. & BENNETT, P. C. 2013. Pore-scale trapping of supercritical CO2 and the role of grain wettability and shape. *Geophysical Research Letters,* 40**,** 3878-3882.

CONN, C. A., MA, K., HIRASAKI, G. J. & BISWAL, S. L. 2014. Visualizing oil displacement with foam in a microfluidic device with permeability contrast. *Lab on a Chip*.

CRAIG, F. F. 1971. *The Reservoir Engineering Aspects of Waterflooding*.

DAVIS, J. A., JR. & JONES, S. C. 1968. Displacement Mechanisms of Micellar Solutions.

DECHSIRI, C., GHIONE, A., VAN DE WIEL, F., DEHLING, H. G., PAANS, A. M. J. & HOFFMANN, A. C. 2005. Positron emission tomography applied to fluidization engineering. *Canadian Journal of Chemical Engineering,* 83**,** 88-96.

DEGUELDRE, C., PLEINERT, H., MAGUIRE, P., LEHMAN, E., MISSIMER, J., HAMMER, J., LEENDERS, K., BOCK, H. & TOWNSEND, D. 1996. Porosity and pathway determination in crystalline rock by positron emission tomography and neutron radiography. *Earth and Planetary Science Letters,* 140**,** 213-225.

DULLIEN, F. A. L. 1991. *Porous Media: Fluid Transport and Pore Structure*, Academic Press.

ENICK, R. M. & OLSEN, D. K. 2012. Mobility and Conformance Control for Carbon Dioxide Enhanced Oil Recovery (CO2-EOR) via Thickeners, Foams, and Gels – A Detailed Literature Review of 40 Years of Research. National Energy Technology Laboratory (NETL).

FALLS, A. H., HIRASAKI, G. J., PATZEK, T. W., GAUGLITZ, D. A., MILLER, D. D. & RATULOWSKI, T. 1988. Development of a Mechanistic Foam Simulator: The Population Balance and Generation by Snap-Off.

FERNØ, M. A., GRØNSDAL, R., ÅSHEIM, J., NYHEIM, A., BERGE, M. & GRAUE, A. 2011. Use of Sulfate for Water Based Enhanced Oil Recovery during Spontaneous Imbibition in Chalk. *Energy Fuels,* 25**,** 1697-1706.

FJELDE, I., ZUTA, J. & DUYILEMI, O. V. 2008. Oil Recovery from Matrix during CO2-Foam Flooding of Fractured Carbonate Oil Reservoirs. Society of Petroleum Engineers.

GRIGG, R. B. & SCHECHTER, D. S. 1997. State of the Industry in CO2 Floods. Society of Petroleum Engineers.

GUNTER, W. D., WIWEHAR, B. & PERKINS, E. H. 1997. Aquifer disposal of CO2-rich greenhouse gases: Extension of the time scale of experiment for CO2-sequestering reactions by geochemical modelling. *Mineralogy and Petrology,* 59**,** 121-140.

GUPTA, R., SMITH, G. G., HU, L., WILLINGHAM, T., LO CASCIO, M., SHYEH, J. J. & HARRIS, C. R. 2011. Enhanced Waterflood for Carbonate Reservoirs - Impact of Injection Water Composition. Society of Petroleum Engineers.

HAUGAN, A. A Low-Cost PET System for Use in Flow Experiments of Porous Media. SPE Annual Technical Conference and Exhibition, 1-4 October 2000 Dallas, Texas.

HAUGEN, Å., FERNØ, M. A., GRAUE, A. & BERTIN, H. J. 2012. Experimental Study of Foam Flow in Fractured Oil-Wet Limestone for Enhanced Oil Recovery.

HEINDEL, T. J. 2011. A Review of X-Ray Flow Visualization With Applications to Multiphase Flows. *Journal of Fluids Engineering-Transactions of the Asme,* 133.

HIRASAKI, G., MILLER, C. A. & PUERTO, M. 2011. Recent Advances in Surfactant EOR.

HIRASAKI, G. J. & LAWSON, J. B. 1985. Mechanisms of Foam Flow in Porous Media: Apparent Viscosity in Smooth Capillaries.

HOFF, W. D., WILSON, M. A., BENTON, D. M., HAWKESWORTH, M. R., PARKER, D. J. & FOWLES, P. 1996. The use of positron emission tomography to monitor

unsaturated water flow within porous construction materials. *Journal of Materials Science Letters,* 15**,** 1101-1104.

HOLM, L. W. 1968. The Mechanism of Gas and Liquid Flow Through Porous Media in the Presence of Foam.

HORNBROOK, J. W., CASTANIER, L. M. & PETTIT, P. A. 1991. Observation of Foam/Oil Interactions in a New, High-Resolution Micromodel. Society of Petroleum Engineers.

HOTEIT, H. & FIROOZABADI, A. 2009. Numerical Modeling of Diffusion in Fractured Media for Gas-Injection and -Recycling Schemes.

HUH, D. G., COCHRANE, T. D. & KOVARIK, F. S. 1989. The Effect of Microscopic Heterogeneity on CO2-Foam Mobility: Part 1--Mechanistic Study.

IGLAUER, S., PALUSZNY, A., PENTLAND, C. H. & BLUNT, M. J. 2011. Residual CO2 imaged with X-ray micro-tomography. *Geophysical Research Letters,* 38**,** L21403.

IKEDA, T., KOTANI, K., MAEDA, Y. & KOHNO, H. 1983. Preliminary-Study on Application of X-Ray Ct Scanner to Measurement of Void Fractions in Steady-State 2-Phase Flows. *Journal of Nuclear Science and Technology,* 20**,** 1-12.

KHALILI, A., BASU, A. J. & PIETRZYK, U. 1998. Flow visualization in porous media via Positron Emission Tomography. *Physics of Fluids,* 10**,** 1031-1033.

KHATIB, Z. I., HIRASAKI, G. J. & FALLS, A. H. 1988. Effects of Capillary Pressure on Coalescence and Phase Mobilities in Foams Flowing Through Porous Media.

KIM, Y., WAN, J., KNEAFSEY, T. J. & TOKUNAGA, T. K. 2012. Dewetting of silica surfaces upon reactions with supercritical CO2 and brine: pore-scale studies in micromodels. *Environ Sci Technol,* 46**,** 4228-35.

KINAHAN, P. E., TOWNSEND, D. W., BEYER, T. & SASHIN, D. 1998. Attenuation correction for a combined 3D PET/CT scanner. *Med Phys,* 25**,** 2046-53.

KOVSCEK, A. R., TANG, G. Q. & RADKE, C. J. 2007. Verification of Roof snap off as a foam-generation mechanism in porous media at steady state. *Colloids and Surfaces A: Physicochemical and Engineering Aspects,* 302**,** 251-260.

KOVSCEK, A. R., TRETHEWAY, D. C., PERSOFF, P. & RADKE, C. J. 1995. Foam flow through a transparent rough-walled rock fracture. *Journal of Petroleum Science and Engineering,* 13**,** 75-86.

KREVOR, S. C. M., PINI, R., ZUO, L. & BENSON, S. M. 2012. Relative permeability and trapping of CO2 and water in sandstone rocks at reservoir conditions. *Water Resources Research,* 48**,** W02532.

KULENKAMPFF', J., GRUUNDIG, M., RICHTER, M. & ENZMANN, F. 2008. Evaluation of positron-emission-tomography for visualisation of migration processes in geomaterials. *Physics and Chemistry of the Earth,* 33**,** 937-942.

KULKARNI, M. M. & RAO, D. N. 2004. Experimental Investigation of Various Methods of Tertiary Gas Injection. Society of Petroleum Engineers.

LAGER, A., WEBB, K. J., COLLINS, I. R. & RICHMOND, D. M. 2008. LoSal Enhanced Oil Recovery: Evidence of Enhanced Oil Recovery at the Reservoir Scale. Society of Petroleum Engineers.

LAKE, L. W. 1989. *Enhanced Oil Recovery*, Englewood Cliffs, N.J. : Prentice Hall.

LAMBERT, M. R., MARINO, S. D., ANTHONY, T. L., CALVIN, M. W., GUTIERREZ, S. & SMITH, D. P. 1996. Implementing CO2 Floods: No More Delays! : Society of Petroleum Engineers.

LAWSON, J. B. & REISBERG, J. 1980. Alternate Slugs Of Gas And Dilute Surfactant For Mobility Control During Chemical Flooding. Society of Petroleum Engineers.

LEE, D., HERMAN, J., ELSWORTH, D., KIM, H. & LEE, H. 2011. A critical evaluation of unconventional gas recovery from the marcellus shale, northeastern United States. *KSCE Journal of Civil Engineering,* 15**,** 679-687.

LI, R. F., HIRASAKI, G. J., MILLER, C. A. & MASALMEH, S. K. 2011. Wettability Alteration and Foam Mobility Control in a Layered 2-D Heterogeneous System. Society of Petroleum Engineers.

LI, R. F., YAN, W., LIU, S., HIRASAKI, G. & MILLER, C. A. 2010. Foam Mobility Control for Surfactant Enhanced Oil Recovery.

LINDEBERG, E. & HOLT, T. 1994. EOR by Miscible CO2 Injection in the North Sea. Society of Petroleum Engineers.

LINDEBERG, E. & WESSEL-BERG, D. 1997. Vertical convection in an aquifer column under a gas cap of CO2. *Energy Conversion and Management,* 38, Supplement**,** S229-S234.

LLAVE, F. M., CHUNG, F. T. H., LOUVIER, R. W. & HUDGINS, D. A. 1990. Foams as Mobility Control Agents for Oil Recovery by Gas Displacement. Society of Petroleum Engineers.

MAGUIRE, R. P., MISSIMER, J. H., EMERT, F., TOWNSEND, D. W., DOLLINGER, H. & LEENDERS, K. L. 1997. Positron emission tomography of large rock samples using a multiring PET instrument. *Ieee Transactions on Nuclear Science,* 44**,** 26-30.

MAST, R. F. 1972. Microscopic Behavior of Foam in Porous Media. Society of Petroleum Engineers.

MATTAX, C. C. & KYTE, J. R. 1961. Ever see a water flood. *The Oil and Gas Journal***,** 115-128.

MCGUIRE, P. L., CHATHAM, J. R., PASKVAN, F. K., SOMMER, D. M. & CARINI, F. H. 2005. Low Salinity Oil Recovery: An Exciting New EOR Opportunity for Alaska's North Slope. Society of Petroleum Engineers.

MORROW, N. & BUCKLEY, J. 2011. Improved Oil Recovery by Low-Salinity Waterflooding. *Journal of Petroleum Technology,* 63.

NGUYEN, Q. P., CURRIE, P. K. & ZITHA, P. L. J. 2003. Effect of Capillary Cross-Flow on Foam-Induced Diversion in Layered Formations. Society of Petroleum Engineers.

OGILVIE, S. R., ORRIBO, J. M. & GLOVER, P. W. J. 2001. The influence of deformation bands upon fluid flow using profile permeametry and positron emission tomography. *Geophysical Research Letters,* 28**,** 61-64.

OKASHA, T. M. & ALSHIWAISH, A. 2009. Effect of Brine Salinity on Interfacial Tension in Arab-D Carbonate Reservoir, Saudi Arabia. Society of Petroleum Engineers.

OLDENBURG, C. M., PRUESS, K. & BENSON, S. M. 2001. Process Modeling of CO2 Injection into Natural Gas Reservoirs for Carbon Sequestration and Enhanced Gas Recovery. *Energy & Fuels,* 15**,** 293-298.

OWETE, O. S. & BRIGHAM, W. E. 1987. Flow Behavior of Foam: A Porous Micromodel Study.

PANCHAROEN, M., FERNØ, M. A. & KOVSCEK, A. R. 2012. Modeling foam displacement in fractures. *JOURNAL OF PETROLEUM SCIENCE AND ENGINEERING,* 100**,** 50-58.

PENTLAND, C. H., EL-MAGHRABY, R., IGLAUER, S. & BLUNT, M. J. 2011. Measurements of the capillary trapping of super-critical carbon dioxide in Berea sandstone. *Geophysical Research Letters,* 38**,** L06401.

PERRIN, C. L., TARDY, P. M. J., SORBIE, K. S. & CRAWSHAW, J. C. 2006. Experimental and modeling study of Newtonian and non-Newtonian fluid flow in pore network micromodels. *Journal of Colloid and Interface Science,* 295**,** 542-550.

PHARMAFLUIDICS. 2013. *RE: Personal communication.*

POPE, G. 2011. Recent Developments and Remaining Challenges of Enhanced Oil Recovery. *Journal of Petroleum Technology***,** 65-68.

PU, H., XIE, X., YIN, P. & MORROW, N. R. 2010. Low-Salinity Waterflooding and Mineral Dissolution. Society of Petroleum Engineers.

QI, R., LAFORCE, T. C. & BLUNT, M. J. 2009. Design of carbon dioxide storage in aquifers. *International Journal of Greenhouse Gas Control,* 3**,** 195-205.

RANGEL-GERMAN, E. R. & KOVSCEK, A. R. 2006. A micromodel investigation of two-phase matrix-fracture transfer mechanisms. *Water Resources Research,* 42**,** W03401.

RANSOHOFF, T. C. & RADKE, C. J. 1988. Mechanisms of Foam Generation in Glass-Bead Packs.

ROBIN, M., BEHOT, J. & SYGOUNI, V. 2012. CO2 Injection in Porous Media : Observations un Glass Micromodels Under Reservoir Conditions. Society of Petroleum Engineers.

ROMANUKA, J., HOFMAN, J., LIGTHELM, D. J., SUIJKERBUIJK, B., MARCELIS, F., OEDAI, S., BRUSSEE, N., VAN DER LINDE, H., AKSULU, H. & AUSTAD, T. 2012. Low Salinity EOR in Carbonates. Society of Petroleum Engineers.

ROOF, J. G. 1970. Snap-Off of Oil Droplets in Water-Wet Pores.

ROSENBAUER, R. J. & THOMAS, B. 2010. Carbon dioxide sequestration in deep saline aquifers and formations. *Woodhead Publishing Series in Energy,* 8**,** 57-103.

ROSSEN, W. R. 1996. *Foams in Enhanced Oil Recovery. Foams: Theory, Measurements and Applications*, Marcel Dekker.

ROSSEN, W. R. 1999. Foam Generation at Layer Boundaries in Porous Media.

SANDENGEN, K. & ARNTZEN, O. J. Osmosis During Low Salinity Waterflooding. EAGE IOR - 17th European Symposium on Improved Oil Recovery 2013 St. Petersburg, Russia.

SCHRAMM, L. L. 1994. *Foams: Fundamentals and Applications in the Petroleum Industry*, American Chemical Society.

SECCOMBE, J., LAGER, A., JERAULD, G., JHAVERI, B., BUIKEMA, T., BASSLER, S., DENIS, J., WEBB, K., COCKIN, A. & FUEG, E. 2010. Demonstration of Low-Salinity EOR at Interwell Scale, Endicott Field, Alaska. Society of Petroleum Engineers.

SHABANI AFRAPOLI, M., ALIPOUR, S. & TORSAETER, O. 2011. Fundamental Study of Pore Scale Mechanisms in Microbial Improved Oil Recovery Processes. *Transport in Porous Media,* 90**,** 949-964.

SHAN, D. & ROSSEN, W. R. 2004. Optimal Injection Strategies for Foam IOR.

SIDDIQUI, S., TALABANI, S., YANG, J., SALEH, S. T. & ISLAM, M. R. 2003. An experimental investigation of the diversion characteristics of foam in Berea sandstone cores of contrasting permeabilities. *Journal of Petroleum Science and Engineering,* 37**,** 51-67.

SKJÆVELAND, M. S. & KLEPPE, J. 1992. *SPOR MONOGRAPH - Recent Advances in Improved Oil Recovery Methods for North Sea Sandstone Reservoirs*, Norwegian Petroleum Directorate.

SOROUSH, M., WESSEL-BERG, D., TORSAETER, O. & KLEPPE, J. 2014. Investigating residual trapping in CO2 storage in saline aquifers – application of a 2D glass model, and image analysis. *Energy Science & Engineering,* 2**,** 149-163.

STRAND, S., AUSTAD, T., PUNTERVOLD, T., HØGNESEN, E. J., OLSEN, M. & BARSTAD, S. M. F. 2008. "Smart Water" for Oil Recovery from Fractured Limestone: A Preliminary Study. *Energy & Fuels,* 22**,** 3126-3133.

TAKU IDE, S., JESSEN, K. & ORR JR, F. M. 2007. Storage of CO2 in saline aquifers: Effects of gravity, viscous, and capillary forces on amount and timing of trapping. *International Journal of Greenhouse Gas Control,* 1**,** 481-491.

TANG, G. & MORROW, N. R. 1997. Salinity, Temperature, Oil Composition, and Oil Recovery by Waterflooding. *SPE Reservoir Engineering,* 12**,** 269-276.

TANG, G. & MORROW, N. R. 1999. Influence of brine composition and fines migration on crude oil/brine/rock interactions and oil recovery. *Journal of Petroleum Science and Engineering,* 24**,** 99-111.

TANZIL, D., HIRASAKI, G. J. & MILLER, C. A. 2002. Mobility of Foam in Heterogeneous Media: Flow Parallel and Perpendicular to Stratification. *SPE Journal,* 7**,** 203-212.

TEIGLAND, R. & KLEPPE, J. 2006. EOR Survey in the North Sea. Society of Petroleum Engineers.

TOHIDI, B., ANDERSON, R., CLENNELL, M. B., BURGASS, R. W. & BIDERKAB, A. B. 2001. Visual observation of gas-hydrate formation and dissociation in synthetic porous media by means of glass micromodels. *Geology,* 29**,** 867-870.

TOVAR, F. D., EIDE, O., GRAUE, A. & SCHECHTER, D. S. 2014. Experimental Investigation of Enhanced Recovery in Unconventional Liquid Reservoirs using CO2: A Look Ahead to the Future of Unconventional EOR. Society of Petroleum Engineers.

TURTA, A. T. & SINGHAL, A. K. 2002. Field Foam Applications in Enhanced Oil Recovery Projects: Screening and Design Aspects.

VAN HEERDEN, M., BUFFLER, A., GIBSON, R., STANKIEWICA, M., MAUCEC, M., DUSTERHOFT, R. & RICKMAN, R. D. 2013. Dynamic Imaging of Fluid Mobility in Low-Permeability Rocks Using High-Resolution Positron Emission Tomography. Jakarta, Indonesia: Society of Petroleum Engineers.

WEBB, K. J., BLACK, C. J. J. & AL-AJEEL, H. 2004. Low Salinity Oil Recovery - Log-Inject-Log. Society of Petroleum Engineers.

WEBB, K. J., BLACK, C. J. J. & TJETLAND, G. 2005. A Laboratory Study Investigating Methods for Improving Oil Recovery in Carbonates. International Petroleum Technology Conference.

YAN, W., MILLER, C. A. & HIRASAKI, G. J. 2006. Foam sweep in fractures for enhanced oil recovery. *Colloids and Surfaces A: Physicochemical and Engineering Aspects,* 282–283**,** 348-359.

YOUSEF, A. A., AL-SALEH, S. & AL-JAWFI, M. S. 2011. New Recovery Method for Carbonate Reservoirs Tagged Smart WaterFlooding. *20th World Petroleum Congress.* Doha, Qatar.

YOUSEF, A. A., AL-SALEH, S. & AL-JAWFI, M. S. 2012. Improved/Enhanced Oil Recovery from Carbonate Reservoirs by Tuning Injection Water Salinity and Ionic Content. Society of Petroleum Engineers.

ZHOU, X., MORROW, N. R. & MA, S. 2000. Interrelationship of Wettability, Initial Water Saturation, Aging Time, and Oil Recovery by Spontaneous Imbibition and Waterflooding.

4. Appendix – Microfluidic Laboratory Description

The process of building the microfluidic laboratory at University of Bergen (UiB) was initiated the summer of 2011. Today's areas of interest within pore-scale research at UiB include various EOR methods and natural gas production from hydrate-bearing formations. The laboratory holds two permanent setups that are briefly described here.

Setup A consists of an inverted Nikon Eclipse Ti-U microscope with four objective lenses (2x, 5x, 10x, 20x), and green and blue fluorescence filter cubes with individual exciter, emitter and dichroic beamsplitter. In addition, the microscope has a built-in 1.5x zoom, thus making a 30x magnification possible. Fields of view for different objective lenses are given in Table A- 1. A TI-FL Epi-fl illuminator with neutral density (ND)-4 and ND-8 filters was placed behind the microscope body, able to extend fluorescence lifetime by reducing light intensity. An external adjustable light source was connected to the microscope via optical fiber cable. A 5-megapixel, CCD high-definition color camera was used for capturing images of up to 2560 x1920 pixels with 16 bit RGB pixel depth. Time-lapse image sequences were controlled and analyzed in an image acquisition software, and a capture rate of 1 frame per second was achieved with 1280 x 960 pixels at 8bit RGB pixel depth. Setup A also include a Nexus 3000 syringe pump with 23.03 mm ID and step resolution of 0.012 microns (min. flow rate is 0.0023 cm^3/h), a mass flow controller (MFC), and a differential pressure transducer with full scale (FS) 15 bar ± 0.01%FS.

Setup B consists of a Nikon SMZ 1500 microscope, LED-F1 cold light source, Nikon D7100 camera, Quizix SP-5200 pump system, Grant LTC6-30 refrigerated circulating bath, and a closed Plexiglas container system for fluid circulation. The micromodel and the holder are placed within the inner container and the effective temperature can be set from -2 degrees C to +60 degrees C. Maximum absolute pressure using 1.7 mm micromodels is 100 bar.

Table A- 1 – Field of view for different objective lenses for Nikon Eclipse Ti-U

Objective lens	Field of View	
	Width [µm]	Height [µm]
2x zoom	6167.3	4629.6
5x zoom	2470.3	1854.3
10x zoom	1238.5	929.7
20x zoom	626.9	470.6

4.1 Micromodel Manufactering

A feasibility study using a maskless technology to manufacture carbonate etched-silicon micromodels was conducted at UiB NanoStructures Laboratory. In the process, a 180 nm thick layer of a polymethyl methacrylate (PMMA) was deposited on a silicon wafer spinning at 3000 rpm. The sample was then pre-baked on a hotplate. The modified pore geometry was based on an Edward limestone thin-section and transferred to the silicon wafer using an electron beam lithography tool. This technique enabled accurate writing of pore features directly on the PMMA-coated wafer, eliminating the need of an expensive mask. Maximum resolution was about 20 nm on a 100 µm writefield. Electron beams with pre-calibrated exposure dose weakened the positive resist and the sample was developed by removing exposed PMMA that later would represent pore space in the micromodel. Finally, the sample was exposed to plasma etching (CHF_3) in order to transfer the pore geometry from the resist to the silicon wafer. The anisotropic etching created vertical sidewalls in the wafer in areas where the PMMA was removed. PMMA-coated areas (grains) were also slowly destroyed in the process, thus restraining the pore etching depth in the micromodel. The etching process is illustrated in Figure A- 1. Here, a uniform

etching depth of 50 nm was achieved in the silicon wafer. The damaged PMMA layer can be observed in the left image.

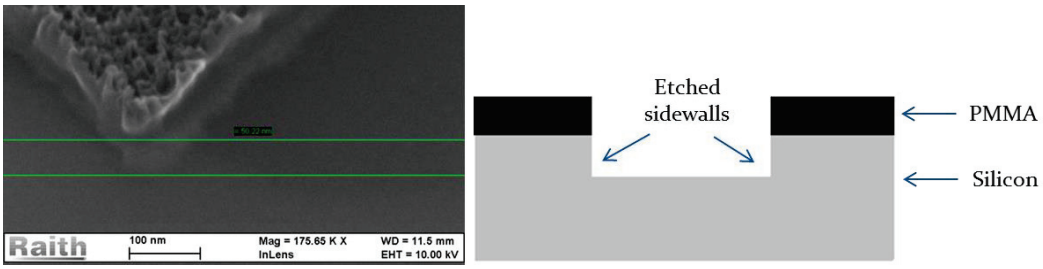

Figure A- 1 – SEM image (left) and cross-sectional illustration (right) of the etching process in the PMMA-coated silicon wafer

4.2 Standard Operating Procedure

Here, a procedure on how to optimize the instalment of the micromodel in the model holder and how to properly seal the system for high-pressure experiments is detailed.

1. Micromodel and fittings/tubes must be thoroughly cleaned using isopropanol and deionized water, and dried prior to the experiment
2. Four identical gaskets (N-124-02) yielding 0.5 mm thickness should be thoroughly centered on the coned female nanoports using flat tip tweezers and pressed into the circular slit
3. Carefully place the micromodel in the squared track with the silicon side facing the seals and coned ports. When installed, the micromodel should be perfectly horizontal and leveled slightly above the top half of the aluminum holder
4. Embed the micromodel in the aluminum holder using a torque key and apply a momentum of 0.5 Nm on the 1.7 mm thick models
5. Coned male nuts and 360 µm OD capillary tubes should be finger-tightened to the female nanoports located on the micromodel holder

6. When all pipelines are connected, pre-flush the system with deionized water at low flow rates
7. Initially, the injection port and the three production ports should be kept open. After water breakthrough, close off individual production ports and inject diagonally across the network. When a 100% water saturated pore network is achieved (confirm visually using the microscope), close the final production port and monotonically pressurize the system using constant pressure operations on the injection pump
8. Select an appropriate field of view and focus the microscope by adjusting the working distance and apply fluorescent filters if needed
9. Initiate the desired displacement process at experimental conditions and obtain microvisual data by choosing relevant temporal resolution (image series or video) on the digital camera embedded on the microscope. Camera should be set to 1/8 shutter speed, ISO 2000, and f/13 aperture

4.3 Osmotic Gradient Induced Oil Recovery in Micromodels

This section describes a standard experimental procedure on osmosis as a low salinity oil recovery mechanism in etched-silicon micromodels. The aforementioned laboratory setup A was used for this project. Brine composition and oil type utilized in various experiments are listed in Table A- 2.

Table A- 2– Fluid composition utilized in osmotic gradient induced oil recovery experiments

	Oil			
Name	**Oil A**	**Oil B**	**Oil C**	**Oil E**
Comp.	n-Hexane	n-Heptane	n-Hexane + 2vol% crude	Ekofisk crude oil
	Water			
Name	**High salinity A**	**High salinity B**	**Low salinity**	
Comp.	5 wt% NaCl	20 wt% NaCl	Deionized water	

Figure A- 2 shows a schematic description of the high-pressure micromodel consisting of a pore network, two fluid distribution channels and four ports located in each corner allowing fluid injection (port 1) and production (port 2, port 4). The micromodel was embedded in an aluminum holder and installed horizontally on the microscope stage. The porous medium was prepared by the following five steps: 1) *Initial water saturation.* High salinity water was injected through port 1 into a cleaned, air-filled model until 100% water saturation was achieved within the porous network and distribution channels. Air was displaced by water by a combination of spontaneous and forced imbibition, and production occurred through port 2 and/or port 4.

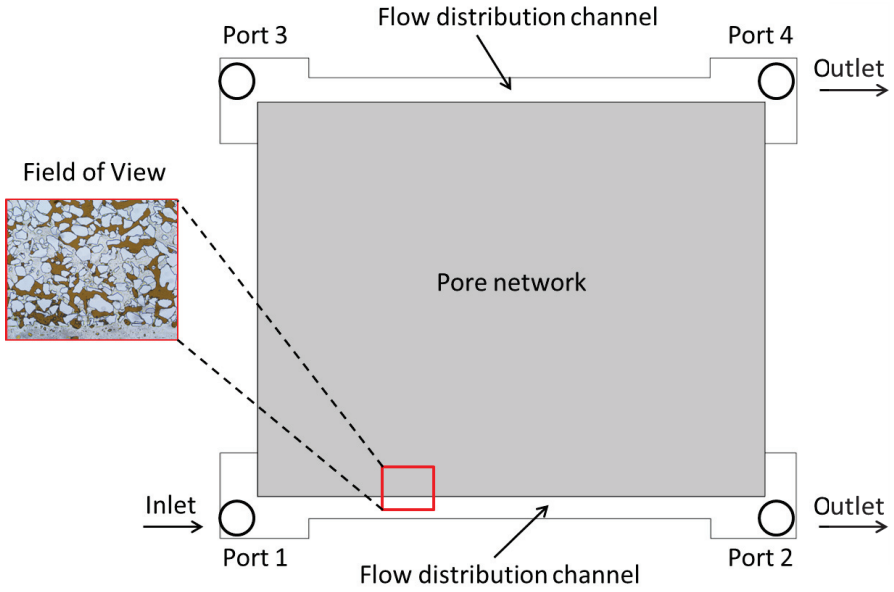

Figure A- 2 – Schematic description of the micromodel including injection/production ports, flow distribution channels and pore network. Field of view is indicated in the transition area between the channel and the network

2) *Oil primary drainage*. Initially, oil displaced saline formation water from port 1 to port 2. Oil pressure was monotonically increased, and the non-wetting

phase invaded the pore network when the matrix threshold pressure was exceeded. The primary drainage process was terminated when the lower part of the network reached irreducible water saturation. The upper part of the network consisted mostly of formation water. The displacement was monitored through the microscope to make sure a continuous uniform layer of oil was established that acted as a semi-permeable membrane during osmosis later on.

3) *High salinity waterflood*. Oil was displaced from the distribution channel, and high salinity water was injected until spontaneous imbibition ceased in the pore network. Port 3 and 4 were closed during the process. 4) *Low salinity preparation*. An osmotic gradient was established by carefully filling the distribution channel with low salinity water. No oil production occurred at this point. 5) *Water diffusion*. Formation water in the pore network was separated from the low salinity water occupying the channel by a uniform oil layer. Water transportation from the channel towards the pore network occurred in the absence of viscous forces. Fluid movements within the field of view were documented every 15 minutes for about 10 days.